

Modelling the FRP-concrete delamination by means of an exponential softening law

P. Cornetti*, A. Carpinteri

Department of Structural Engineering and Geotechnics, Politecnico di Torino, Torino, Italy

ARTICLE INFO

Article history:

Received 16 September 2010
Received in revised form
16 February 2011
Accepted 28 February 2011
Available online 9 April 2011

Keywords:

FRP
Debonding
Shear lag models
Fracture mechanics
Cohesive models
Exponential softening

ABSTRACT

Among rehabilitation strategies, bonding of Fibre Reinforced Polymers (FRP) plates is becoming more and more popular, especially for what concerns concrete structures. The performance of the interface between FRP and concrete is one of the key factors affecting the behaviour of the strengthened structure. Up to now, closed-form analytical solutions exist only for the local bond-slip law with linear softening. The aim of the present paper is to show that analytical solutions can be achieved also assuming an exponential decaying softening law. Accordingly, the expressions for the interfacial shear stress distribution and the load-displacement response are derived for the different loading stages. A full parametric analysis of the problem has been performed, highlighting the size effect on the structural behaviour as well as the effects of the bond length, of the FRP stiffness and of the interface cohesive law. A comparison with other analytical models as well as with experimental data available in the literature concludes the paper.

© 2011 Elsevier Ltd. All rights reserved.

1. Introduction

Bonding of FRP has emerged as a wide-spread method for retrofitting existing concrete structures. In this technique, the performance of the FRP-to-concrete interface is of primary importance. The failure mode of FRP-reinforced beams is often directly related to the debonding of the FRP plate from the substrate. The debonding of the plate may take place either from the edge of the FRP strip or from an intermediate flexural crack (for a review, see e.g. [1]). The former failure mode is named *edge debonding*, whereas the latter is usually referred to as *intermediate crack-induced debonding* (IC-debonding, Fig. 1).

In the case of IC-debonding failure [2], the stress state is, up to some extent, similar to that of a single or double pull-push shear test (Fig. 2), where one or two FRP plates are bonded to a concrete block and subjected to a tensile load. Because of its relative simplicity, several experiments as well as theoretical analyses have been concerned with such a test geometry. Experiments [3] show that the principal failure mode is concrete failure under shear, leading to a main crack running a few millimetres beneath the concrete-to-adhesive interface. Thus, the maximum bearable load strongly depends on concrete mechanical properties.

Several models have been proposed to describe the pull-push shear test: among the others, we may cite Wu et al. [4], Yuan

et al. [5], Leung and Yang [6] and references therein. However, an analytical solution for the complete debonding process is available in closed-form only for a local bond-slip law with linear softening (Yuan et al. [5], Leung and Tung [7]). The aim of the present paper is to provide an analytical solution for an exponentially decaying softening of the interfacial stress-displacement law. Up to now, the solution, in the case of a non-linear softening cohesive law, has been achieved only numerically (see, e.g., [8]). Finally, observe that, although the attention is focused on FRP-to-concrete bonded joints, the present analysis is applicable also to other kinds of reinforcement, e.g. steel plates.

2. Governing equations

In Fig. 2 the double and single pull-push shear test geometries are drawn. The first geometry (Fig. 2(a)) can be regarded as a kind of double lap joint. In such a joint, the adhesive layer is mainly subjected to shear deformations, so that mode II interfacial fracture is the expected failure mode. However, note that a rigorous elastic analysis of the problem shows that a mode I component is also present [9], but we will neglect such a contribution since it can be shown [10,11] that peeling stresses at the end of a double lap joint are negligible if the thickness of the outer adherends is small enough.

The single shear test is more common in experiments, since it is more easily feasible. Provided that a positioning frame preventing the concrete block from up-lifting is present (Fig. 2(b)), the stress-strain state in the double and single pull-push

* Corresponding author. Tel.: +39 0115644901; fax: +39 0115644899.
E-mail address: pietro.cornetti@polito.it (P. Cornetti).

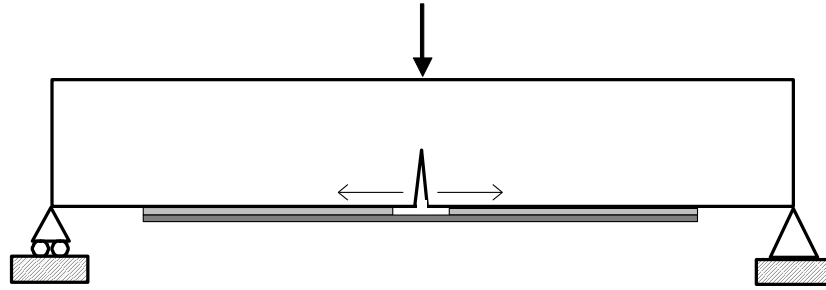


Fig. 1. Intermediate crack-induced (IC) debonding. The thin arrows represent the direction of the debonding crack propagation.

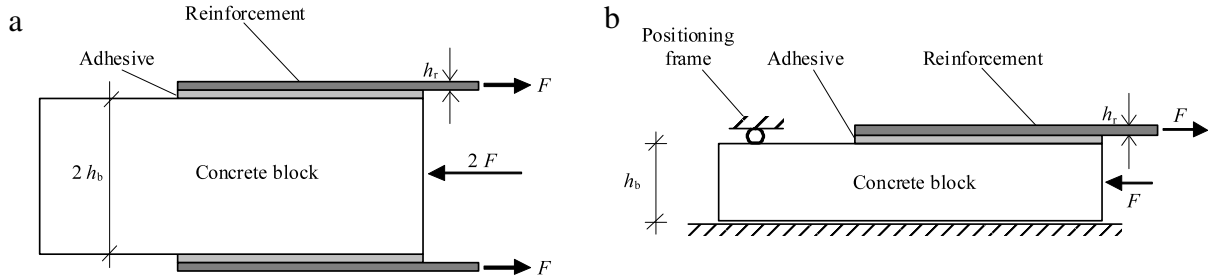


Fig. 2. Double (a) and single (b) pull–push shear test geometries (elevation).

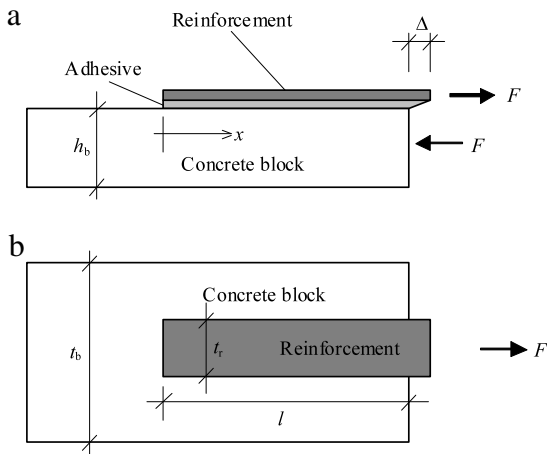


Fig. 3. Single pull–push shear test geometry: (a) elevation; (b) plan. The relative displacement between the concrete block and the loaded end of the FRP plate is denoted by Δ .

shear test geometries is approximately the same and the above considerations about the double shear geometry hold also for the single shear test. Hence, for the sake of simplicity, in the following we will always refer to the single pull–push shear test.

Referring now to Fig. 3, we assume that the width and thickness of each of the three components (plate, adhesive layer and concrete prism) are constant along the length. The width and thickness of the reinforcement plate are denoted respectively by t_r and h_r , those of the concrete prism by t_b and h_b , and the bonded length is denoted by l ; x is the longitudinal coordinate. The Young's moduli of plate and concrete are E_r and E_b , respectively.

According to the previous considerations, a simple mechanical model for the pull–push shear test can be established by treating the plate and the concrete prism (the two adherents) as being subject to axial deformations only, while the adhesive layer can be assumed to be subject to shear deformations only. That is, both adherents are assumed to be subject to uniformly distributed axial stresses, with any bending effects neglected, while the adhesive

layer is assumed to be subject to shear stresses which are also constant across the thickness of the adhesive layer. These kinds of models are usually referred to as *shear lag models*, and its first application, at least in the linear elastic regime, probably dates back to Volkersen [12].

In the case under examination, it should be noted that the adhesive layer represents not only the deformation of the actual adhesive layer, but also that of the materials adjacent to the adhesive. Based on these assumptions, the equilibrium equations of the reinforcement and of the overall specimen cross section read respectively:

$$h_r \frac{d\sigma_r}{dx} - \tau = 0 \quad (1)$$

$$\sigma_r h_r t_r + \sigma_b h_b t_b = 0 \quad (2)$$

where τ is the shear stress in the adhesive layer, σ_r is the axial stress in the reinforcement plate and σ_b is the axial stress in the concrete prism. The constitutive equations for the adhesive layer and the two adherents are:

$$\tau = \tau(\delta) \quad (3)$$

$$\sigma_r = E_r \frac{du_r}{dx} \quad (4)$$

$$\sigma_b = E_b \frac{du_b}{dx} \quad (5)$$

where u_r and u_b are the longitudinal displacements of the reinforcement and of the concrete, respectively. By means of Eqs. (1)–(5), it is possible to achieve the following second order differential equation in the interfacial slip δ , defined as the relative displacement between the two adherents (i.e. $\delta = u_r - u_b$):

$$\frac{d^2\delta}{dx^2} - \frac{1+\rho}{E_r h_r} \tau(\delta) = 0 \quad (6)$$

where ρ is the mechanical fraction of reinforcement (i.e. $\rho = E_r t_r h_r / E_b t_b h_b$). Observe that, by Eq. (2) and by the definition of slip, it is possible to express the stress in the FRP as a function of the first derivative of the slip:

$$\sigma_r = \frac{E_r}{1+\rho} \frac{d\delta}{dx} \quad (7)$$

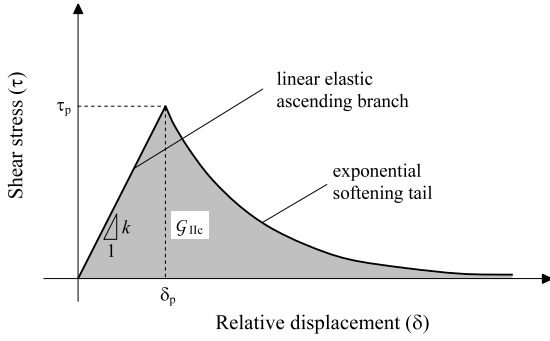


Fig. 4. Local bond-slip model with exponential softening. The peak stress is denoted by τ_p , while δ_p is the corresponding relative displacement; k is the slope of the linear elastic branch. The grey area beneath the curve corresponds to the mode II fracture energy \mathcal{G}_{IIc} .

3. Cohesive law of the interface

An analytical solution based on a linear softening bond-slip law was presented in [5]. However, the linear softening law is often not realistic; furthermore, as it will be shown later, its use can lead to overestimating the mechanical properties of the joint. Among the different interfacial laws available in the literature, we will use the one (Fig. 4) recently proposed by Neale et al. [13] on the basis of the analysis presented in [14], characterised by a linear phase, with slope k , followed by an exponential softening branch. In formulae:

$$\tau = \tau(\delta) = \begin{cases} k\delta, & \text{if } 0 \leq \delta \leq \delta_p \\ \tau_p e^{-2\alpha^2(\delta/\delta_p - 1)}, & \text{if } \delta \geq \delta_p \end{cases} \quad (8)$$

where τ_p is the peak shear stress, δ_p the related slip, k the slope of the elastic ascending branch ($k = \tau_p/\delta_p$) and α^2 is a (positive) coefficient characterising the exponential decay. The area beneath the curve represents the interface mode II fracture energy \mathcal{G}_{IIc} :

$$\mathcal{G}_{IIc} = \int_0^{\infty} \tau(\delta) d\delta = \frac{\tau_p \delta_p}{2} \left(1 + \frac{1}{\alpha^2} \right). \quad (9)$$

Note that the bond-slip law is univocally defined once three quantities among k , τ_p , δ_p , α^2 , \mathcal{G}_{IIc} are given. Introducing the dimensionless relative displacement $y = \delta/\delta_p$, the bond-slip can be set in dimensionless form as:

$$\frac{\tau}{\tau_p} = f(y) = \begin{cases} y, & \text{if } 0 \leq y \leq 1 \\ e^{-2\alpha^2(y-1)}, & \text{if } y \geq 1. \end{cases} \quad (10)$$

As limit cases, observe that, for $\alpha \rightarrow \infty$, the cohesive law (8) represents an elastic-perfectly brittle interface, whereas, for $\alpha \rightarrow 0$, it represents an elastic-perfectly plastic interface. Furthermore, from Eq. (9) it is evident that α^2 represents the ratio of the area beneath the straight line to the area beneath the exponential branch.

4. Analysis of the debonding process

In order to solve Eq. (6), it is more convenient to use a dimensionless formulation. The longitudinal coordinate is normalised with respect to the bond length l , i.e. $\xi = x/l$. Hence, in Eq. (6), δ and x may be replaced by y and ξ respectively, yielding:

$$\frac{d^2 y}{d\xi^2} - \beta^2 f(y) = 0 \quad (11)$$

where $y(\xi)$ is the unknown function and:

$$\beta = l \sqrt{\frac{1 + \rho}{E_r h_r}} k \quad (12)$$

is a dimensionless parameter depending on geometry and on elastic constants of the materials and of the interface.

Before starting to analyse the different stages of the debonding process, it is worth recalling that, for a given set of material and geometrical parameters, the failure load is a monotonically increasing function of the bond length l . However, for a bond length tending to infinity, it can be proved that the failure load tends to the following asymptotic value:

$$F_c^\infty = t_r \sqrt{\frac{2\mathcal{G}_{IIc} E_r h_r}{1 + \rho}}. \quad (13)$$

In other words, F_c^∞ represents the maximum force that the FRP plate can transfer and can be directly obtained applying Linear Elastic Fracture Mechanics (LEFM) to the pull-push geometry under the assumption of a rigid-perfectly brittle behaviour of the interface (see Appendix D for details). Here we wish to emphasise that the maximum transferable force depends only on the fracture energy, i.e. it does not depend on the shape of the interfacial cohesive law. Furthermore, observe that the presence of the limit value F_c^∞ is peculiar of external reinforcements. In fact, for internal reinforcing bars, there is always an anchorage length above which the full tensile strength of the reinforcement can be exploited.

The pull-push shear test is characterised by the load vs. displacement curve. The displacement of the bonded joint is defined as the slip at the loaded end (i.e. the value of δ at $x = l$) and is denoted by Δ . Hence:

$$\frac{\Delta}{\delta_p} = y(1). \quad (14)$$

The force F at the loaded end of the reinforcement may be evaluated by means of Eq. (7) as $F = t_r h_r \sigma_r(x = l)$. By normalising the force with respect to the maximum transferable force (13) and through analytical manipulations, we get:

$$\frac{F}{F_c^\infty} = \frac{\alpha}{\beta \sqrt{1 + \alpha^2}} y'(1). \quad (15)$$

Eqs. (14) and (15) define the parametric plot of the load vs. displacement curve.

4.1. Elastic stage

During the elastic stage, all the interface is in the elastic regime, i.e. $y < 1$ for any ξ . We may prescribe that, at the loaded end, the dimensionless displacement $y(1)$ is equal to u , with $0 < u < 1$. According to linear elasticity, this setting is equivalent to imposing that the shear stress at the loaded end divided by the peak stress, i.e. $\tau(l)/\tau_p$, is equal to u . The second boundary condition states that the other edge of the reinforcement is unloaded, i.e. $y'(0) = 0$ because of Eq. (7). In formulae:

$$\begin{cases} y'' - \beta^2 y = 0, & 0 \leq \xi \leq 1 \\ y'(0) = 0 \\ y(1) = u, & 0 \leq u \leq 1. \end{cases} \quad (16)$$

The general solution of the (linear) differential equation reads:

$$y(\xi) = c_1 e^{\beta \xi} + c_2 e^{-\beta \xi}. \quad (17)$$

The two arbitrary constants have to be determined by means of the boundary conditions. Hence:

$$y(\xi) = \frac{\cosh(\beta \xi)}{\cosh(\beta)} u = \frac{\tau(\xi)}{\tau_p} \quad (18)$$

$$y'(\xi) = \beta \frac{\sinh(\beta \xi)}{\cosh(\beta)} u. \quad (19)$$

Because of the elastic regime, the relative displacement (18) also represents the shear stress. For $u = 0.5$ (and $\beta = 3$), the shear stress in the adhesive layer and the axial stress in the FRP are represented by curves A in Fig. 5(a) and (b), respectively.

By means of Eqs. (14)–(15) and (18)–(19), the parametric plot of the load vs. displacement curve in the elastic regime is therefore given by:

$$\begin{cases} \frac{\Delta}{\delta_p} = u \\ \frac{F}{F_c^\infty} = \frac{\alpha}{\sqrt{1 + \alpha^2}} \tanh(\beta)u \end{cases} \quad (20)$$

where the parameter u ranges from 0 to 1.

4.2. Elastic-softening stage

At the end of the elastic stage, the shear stress reaches its peak at the loaded end of the joint. Although the structural behaviour of the joint depends on the test control, we assume as the control parameter the position of the stress peak in order to obtain all the possible solutions satisfying the governing Eq. (11). In other words, we make the assumption that the stress peak travels from the loaded end to the unloaded extreme. Let us denote that position with $\bar{\xi}$. It divides the bonded length into two regions: the former ($0 < \xi < \bar{\xi}$) is in the elastic regime, the latter is in the softening regime ($\bar{\xi} < \xi < 1$). Since, at the peak, y is equal to unity, the differential problem governing the solution of the elastic zone is:

$$\begin{cases} y'' - \beta^2 y = 0, & 0 \leq \xi \leq \bar{\xi} < 1 \\ y'(0) = 0 \\ y(\bar{\xi}) = 1. \end{cases} \quad (21)$$

The general solution is still given by Eq. (17). However, because of the different boundary conditions, the solution now reads:

$$y(\xi) = \frac{\cosh(\beta\xi)}{\cosh(\beta\bar{\xi})} = \frac{\tau(\xi)}{\tau_p} \quad (22)$$

$$y'(\xi) = \beta \frac{\sinh(\beta\xi)}{\cosh(\beta\bar{\xi})}. \quad (23)$$

Between the point ($\xi = \bar{\xi}$) where the shear stress reaches its peak and the loaded end ($\xi = 1$), the interface is in the softening regime: the differential equation changes accordingly and it is not linear any more. On the other hand, the boundary conditions are given by the continuity conditions (respectively for the relative displacement and the tensile force in the reinforcement) with the zone in the elastic regime and can therefore be obtained by evaluating Eqs. (22)–(23) at $\xi = \bar{\xi}$:

$$\begin{cases} y'' - \beta^2 e^{-2\alpha^2(y-1)} = 0, & 0 < \bar{\xi} \leq \xi \leq 1 \\ y(\bar{\xi}) = 1 \\ y'(\bar{\xi}) = \beta \tanh(\beta\bar{\xi}). \end{cases} \quad (24)$$

Analytical details about how to achieve the solution of the differential problem (24) are provided in Appendix A. The final solution reads:

$$y(\xi) = 1 + \frac{1}{\alpha^2} \ln \frac{\cosh\{\alpha\beta\gamma(\xi - \bar{\xi}) + \ln[\gamma + \alpha \tanh(\beta\bar{\xi})]\}}{\cosh\{\ln[\gamma + \alpha \tanh(\beta\bar{\xi})]\}} \quad (25)$$

$$y'(\xi) = \frac{\beta\gamma}{\alpha} \tanh\{\alpha\beta\gamma(\xi - \bar{\xi}) + \ln[\gamma + \alpha \tanh(\beta\bar{\xi})]\} \quad (26)$$

with $\gamma = [\alpha^2 \tanh^2(\beta\bar{\xi}) + 1]^{1/2}$. From Eq. (25), it is evident that $y = 1$ for $\xi = \bar{\xi}$ and larger than unity otherwise.

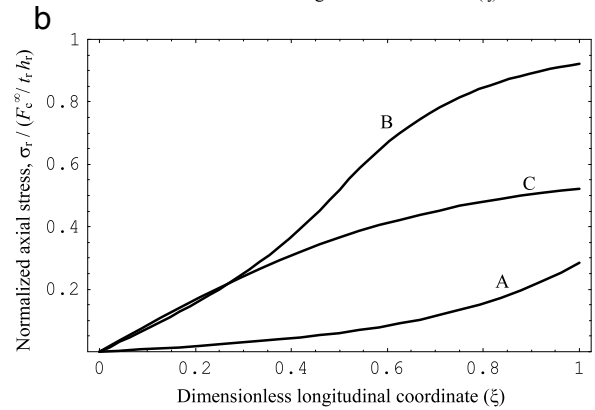
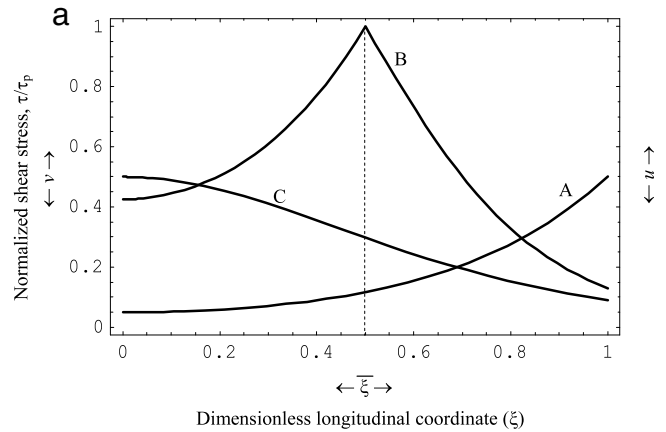


Fig. 5. Shear stress (a) at the interface and axial stress (b) in the FRP ($\alpha = 0.7$, $\beta = 3$): elastic (A), elastic-softening (B) and softening (C) stage; $\xi = 0$ corresponds to the unloaded end and $\xi = 1$ corresponds to the loaded end.

The stress field is obtained upon substitution of Eq. (25) into the constitutive law (10):

$$\frac{\tau(\xi)}{\tau_p} = \left\{ \frac{\cosh[\ln(\gamma + \alpha \tanh(\beta\bar{\xi}))]}{\cosh\{\alpha\beta\gamma(\xi - \bar{\xi}) + \ln(\gamma + \alpha \tanh(\beta\bar{\xi}))\}} \right\}^2. \quad (27)$$

For $\bar{\xi} = 0.5$ (and $\alpha = 0.7$, $\beta = 3$), the shear stress in the adhesive layer and the axial stress in the FRP are represented by curves B in Fig. 5(a) and (b), respectively.

By means of Eqs. (14)–(15) and (25)–(26), the parametric plot of the load vs. displacement curve in the elastic-softening regime is therefore given by:

$$\begin{cases} \frac{\Delta}{\delta_p} = 1 + \frac{1}{\alpha^2} \ln \frac{\cosh\{\alpha\beta\gamma(1 - \bar{\xi}) + \ln[\gamma + \alpha \tanh(\beta\bar{\xi})]\}}{\cosh\{\ln[\gamma + \alpha \tanh(\beta\bar{\xi})]\}} \\ \frac{F}{F_c^\infty} = \frac{\gamma}{\sqrt{1 + \alpha^2}} \tanh\{\alpha\beta\gamma(1 - \bar{\xi}) + \ln[\gamma + \alpha \tanh(\beta\bar{\xi})]\} \end{cases} \quad (28)$$

where the parameter $\bar{\xi}$ ranges from 1 to 0.

4.3. Softening stage

When the peak of the shear stress reaches the unloaded edge of the FRP strip, all the interface is in the softening regime. The maximum shear stress is now fixed at $\xi = 0$; its value is assumed to decrease from τ_p to 0, the latter value corresponding to the complete detachment of the FRP from the concrete substrate. Therefore, the stress field in the softening regime can be obtained by imposing that the normalised shear stress, τ/τ_p , at the unloaded end is equal to the parameter v , with $0 < v < 1$. The boundary condition on the stress may be converted into a displacement

condition by means of the constitutive law (10). Thus, the related differential problem reads:

$$\begin{cases} y'' - \beta^2 e^{-2\alpha^2(y-1)} = 0, & 0 \leq \xi \leq 1 \\ y(0) = 1 - \frac{\ln v}{2\alpha^2}, & 0 < v \leq 1 \\ y'(0) = 0 \end{cases} \quad (29)$$

whose solution is (see Appendix A for details):

$$y(\xi) = 1 + \frac{1}{\alpha^2} \ln \frac{\cosh(\alpha\beta\xi\sqrt{v})}{\sqrt{v}} \quad (30)$$

$$y'(\xi) = \frac{\beta\sqrt{v}}{\alpha} \tanh[\alpha\beta\xi\sqrt{v}]. \quad (31)$$

The stress field is then obtained upon substitution of Eq. (30) into the constitutive law (10):

$$\frac{\tau(\xi)}{\tau_p} = \frac{v}{\cosh^2(\alpha\beta\xi\sqrt{v})}. \quad (32)$$

For $v = 0.5$ (and $\alpha = 0.7$, $\beta = 3$), the shear stress in the adhesive layer and the axial stress in the FRP are represented by curves C in Fig. 5(a) and (b), respectively.

By means of Eqs. (14)–(15) and (30)–(31), the parametric plot of the load vs. displacement curve in the softening regime is therefore given by:

$$\begin{cases} \frac{\Delta}{\delta_p} = 1 + \frac{1}{\alpha^2} \ln \frac{\cosh(\alpha\beta\sqrt{v})}{\sqrt{v}} \\ \frac{F}{F_c^\infty} = \sqrt{\frac{v}{1+\alpha^2}} \tanh[\alpha\beta\sqrt{v}] \end{cases} \quad (33)$$

where the parameter v ranges from 1 to 0.

4.4. Load vs. displacement curve

Eqs. (20), (28) and (33) all together define the parametric plot of the load vs. displacement curve characterising the pull–push shear test. It is interesting to point out that the shape of the dimensionless plot, i.e. F/F_c^∞ vs. Δ/δ_p , depends uniquely on the two dimensionless parameter α and β . The former is related to the parameters of the interfacial cohesive law by the following relationship:

$$\alpha = \left(\frac{2g_{llc}}{\tau_p \delta_p} - 1 \right)^{-1/2} \quad (34)$$

which derives directly from Eq. (9). As already observed, the parameter α is an index of the brittleness of the interface, $\alpha = 0$ corresponding to an elastic-perfectly plastic interfacial behaviour and $\alpha \rightarrow \infty$ to an elastic-perfectly brittle interface.

The latter parameter β is provided by Eq. (12) and depends uniquely on the geometrical dimensions and the elastic properties of the constituent materials. It can be seen as the ratio of the bond length l to a characteristic length l_{ch} of the joint, i.e. $\beta = l/l_{ch}$. The characteristic length is given by:

$$l_{ch} = \sqrt{\frac{E_r h_r}{k(1+\rho)}} \quad (35)$$

i.e. l_{ch} is proportional to the square root of the ratio of the FRP axial stiffness to the shearing stiffness of the interface (up to the factor $1+\rho$, usually very close to unity). Hence, high β values characterise specimens with relatively large bond lengths and/or relatively stiff interfaces.

A typical load vs. displacement curve is plotted in Fig. 6 ($\alpha = 0.7$ and $\beta = 3$). The 01 line corresponds to the elastic regime; the 12 arc to the elastic-softening phase, within which the maximum load

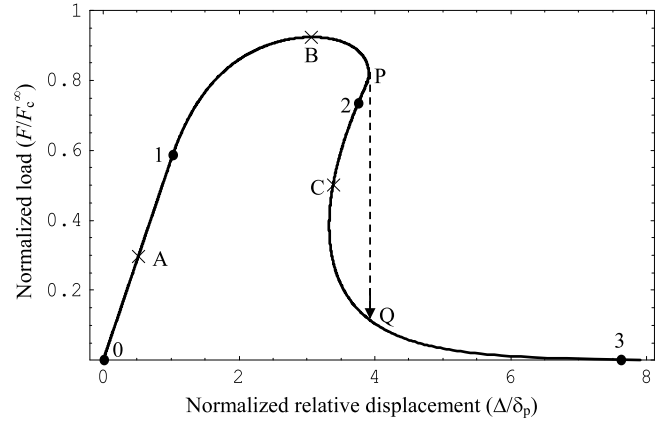


Fig. 6. Typical full-range load–displacement curve ($\alpha = 0.7$, $\beta = 3$): the line 01 corresponds to the elastic stage, the arc 12 to the elastic-softening stage and the branch 23 to the softening phase. The stress field corresponding to points A,B,C are represented by the curves A,B,C in Fig. 5, respectively. The dashed line PQ represents the snap-back occurring if the test is displacement-controlled.

is reached; the 23 branch is attained when all of the interface is in the softening condition. Note that the stress fields corresponding to points A,B,C in Fig. 6 are the ones marked by the same letter in Fig. 5.

It is interesting to observe that, in the example considered in Fig. 6, the application of the simple stress criterion $\tau = \tau_p$ would have provided a failure load (point 1) approximately equal to 2/3 of the actual one (point B). This means that the maximum shear stress may be attained under service loading. On the other hand, the maximum load is achieved when about one half of the bond length is in the softening regime (curve B in Fig. 5). These considerations fully justify the nonlinear analysis herein proposed.

Finally, it is worth observing that, if the test is displacement-controlled, the displacement Δ is monotonically increasing during the test. It means that a snap-back instability [15,16] occurs, i.e. a sudden load drop at fixed displacement from point P to Q (dashed line in Fig. 6). On the other hand, if the test is load-controlled, after the peak load the interfacial crack propagates always unstably up to global failure, i.e. no snap-through may occur.

The presence of the snap-back implies the existence of a region close to the loaded end where the relative displacement (in the softening regime, see Fig. 4) is not monotonically increasing. According to the present analysis it means that, in this region, the shearing stress does not decrease monotonically after its peak has been reached. In other words, the present model assumes the interfacial cohesive law to be reversible. Of course this feature is not realistic, and it may be regarded as a shortcoming of the model. However, it is worth observing that this drawback can be overcome only by defining an unloading law and, consequently, abandoning the analyticity of the solution, which is one of the merits of the present approach. Furthermore, the hypothesis of the reversibility of the interfacial cohesive law affects only the shape of the load–displacement curve between point P and point Q (see Fig. 6), which is considered of minor relevance since it cannot be caught by experimental tests even if they are under displacement control.

5. Comparison with linear softening and LFM models

In the present section we analyse the effect of the parameters α and β on the load vs. displacement curve and compare the response provided by the present approach with the ones obtained by simpler models, namely the linear softening interface model, the LFM model with compliant interface and the LFM model with rigid interface. The corresponding interfacial constitutive laws are

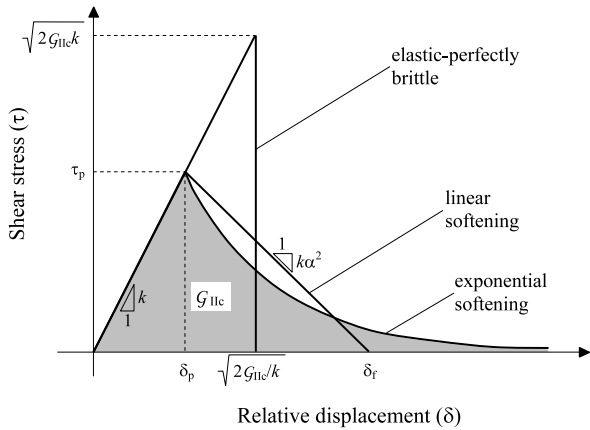


Fig. 7. Local bond–slip models: elastic–perfectly brittle, linear softening, exponential softening laws. The models are compared with the same elastic slope k and the same mode II fracture energy G_{IIc} (i.e. the same area beneath each curve). It follows that the (negative) slope of the linear softening is equal to $k\alpha^2$ and that maximum shearing stress of the elastic–purely brittle law is equal to $\sqrt{2G_{IIc}k}$.

plotted in Fig. 7, whereas the load–displacement curves are given in Figs. 8–9.

In the case of the linear softening interface model the interfacial constitutive law is a piecewise linear function (see Fig. 7) defined as:

$$\tau = \tau(\delta) = \begin{cases} k\delta, & \text{if } 0 \leq \delta \leq \delta_p \\ k[\delta_p - \alpha^2(\delta - \delta_p)], & \text{if } \delta_p \leq \delta \leq \delta_f \\ 0, & \text{if } \delta \geq \delta_f \end{cases} \quad (36)$$

where δ_f is equal to $(1 + 1/\alpha^2) \times \delta_p$. It means that k is the (positive) slope of the elastic branch while $\alpha^2 k$ is the (negative) slope of the softening branch; that is, α^2 is the ratio between the

angular coefficients of the two segments. By defining the slope of the softening branch as $\alpha^2 k$, we have that the area beneath the bond–slip law (36) is still given by Eq. (9). It follows that, provided that k , α^2 and δ_p are the same in Eqs. (8) and (36), both the exponential softening and the linear softening interfacial cohesive law show the same peak stress τ_p and mode II fracture energy G_{IIc} .

As we did for Eq. (8), Eq. (36) can also be cast in dimensionless form as:

$$\frac{\tau}{\tau_p} = f(y) = \begin{cases} y, & \text{if } 0 \leq y \leq 1 \\ 1 - \alpha^2(y - 1), & \text{if } 1 \leq y \leq 1 + 1/\alpha^2 \\ 0, & \text{if } y \geq 1 + 1/\alpha^2. \end{cases} \quad (37)$$

The solution related to the linear softening model is already available in the literature (see, e.g., [5,17]). For the sake of completeness, it is reported in Appendix B with the same notation used in the present paper. From an analytical and numerical point of view it is worth observing that, although linear functions are handled more easily with respect to exponential functions, the solution corresponding to Eq. (37) is more troublesome, since the interface law is defined by three pieces instead of two. In particular, it means that the solution is generally made up of four stages: the elastic one, the elastic–softening one, the elastic–softening–debonding one and the softening–debonding one. Moreover, in the third stage, the relation between the lengths of the three coexisting phases has to be determined numerically. Hence, and differently from the exponential softening model proposed in the present paper, the solution of the linear softening model cannot be claimed to be completely analytical. The reader is referred to Appendix B for further details.

A simpler model is achieved by directly applying LEFM to the pull–push geometry. According to LEFM, the interface is considered to be linear elastic up to failure, i.e. we assume that it has an elastic–perfectly brittle behaviour (see Fig. 7). Therefore

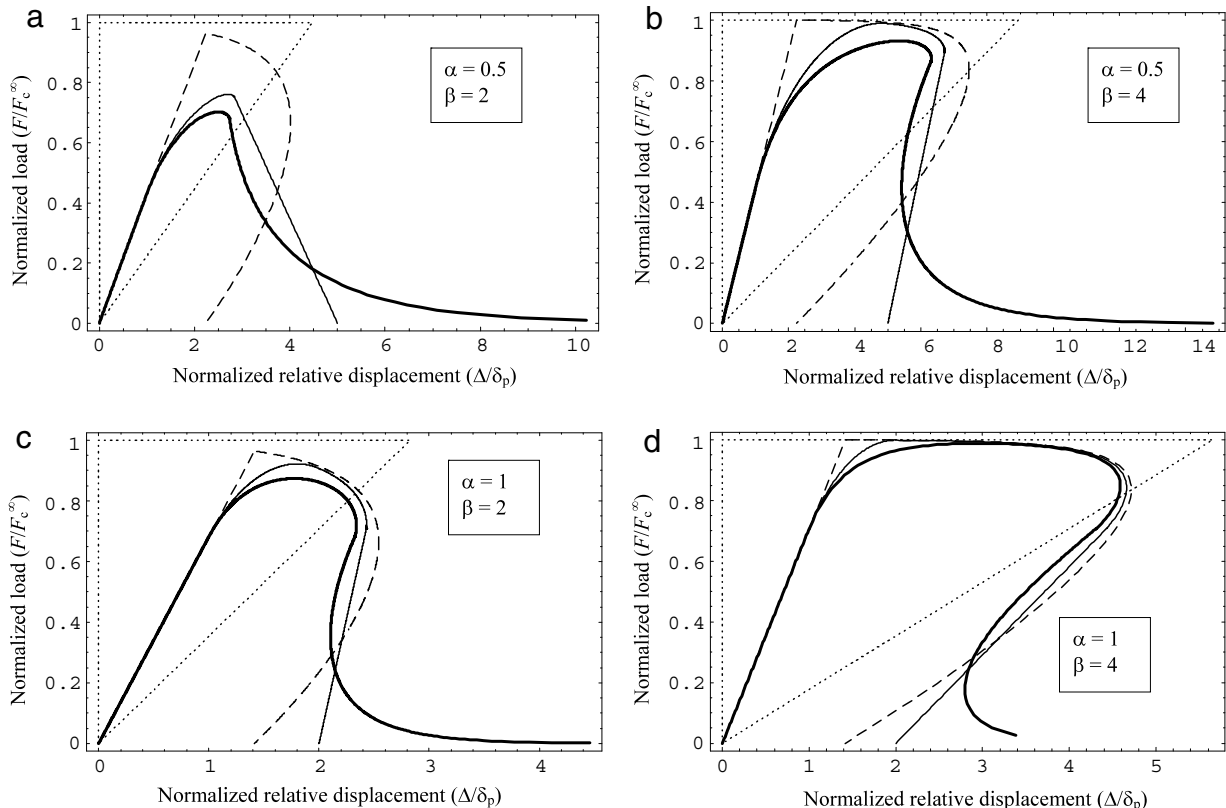


Fig. 8. Dimensionless load–displacement curves according to the different interfacial models: exponential softening (thick line); linear softening (thin line), LEFM model (dashed line), LEFM–EB model (dotted line). Plots from (a) to (d) refer to different values of the dimensionless parameters α and β (see legend).

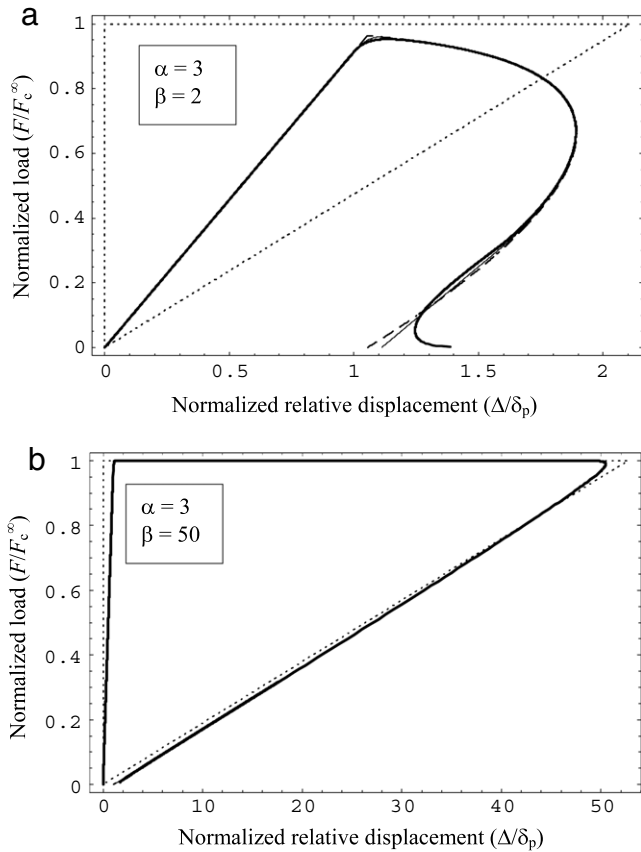


Fig. 9. Dimensionless load–displacement curves according to the different interfacial models: exponential softening (thick line); linear softening (thin line), LEFM model (dashed line), LEFM–EB model (dotted line). For relatively high α values ($\alpha = 3$), the softening models merge with the LEFM model (a). If both α and β attain relatively large values ($\beta = 50$), all the models tend to the LEFM–EB model (b).

LEFM predictions can be achieved by letting α tending to infinity either in the exponential softening model or in the linear softening one. However, the solution provided by LEFM can be more easily achieved by observing that, when the interface is described by a set of linear elastic springs of stiffness k (as in the present case), the strain energy release rate \mathcal{G} is given by [6,18–21]:

$$\mathcal{G} = \frac{\tau_{\max}^2}{2k}. \quad (38)$$

Then, according to LEFM, debonding takes place whenever:

$$\mathcal{G} = \mathcal{G}_{\text{IIc}} \quad (39)$$

i.e. when $\tau_{\max} = \sqrt{2\mathcal{G}_{\text{IIc}}k}$. The failure load can hence be obtained by means of the linear elastic solution (18) and Eqs. (38)–(39). The expressions of the load and displacement values during the delamination process are reported in Appendix C. Note that, according to LEFM, the load vs. displacement plots are represented (dashed lines in Fig. 8) by a straight line up to the debonding onset, corresponding to the maximum load and to a slip equal to $\sqrt{2\mathcal{G}_{\text{IIc}}/k}$ (see Fig. 7), followed by a curve describing how load decreases as the debonding crack propagates. During debonding, the relative displacement Δ firstly increases and then decreases back to the same value $\sqrt{2\mathcal{G}_{\text{IIc}}/k}$ (Fig. 8).

With respect to the previous models, the LEFM one is poorer, in the sense that it needs only two parameters to be defined instead of the three necessary to define either the exponential or the linear softening model. In Fig. 8 we decided to compare the LEFM model with the softening models keeping fixed the slope k of the elastic branch and \mathcal{G}_{IIc} (see Fig. 7), since they are the two parameters that mostly affect the results.

Finally, we considered the predictions obtained by applying LEFM and by assuming, at the same time, a rigid interfacial behaviour ($k \rightarrow \infty$). This hypothesis corresponds to assuming a planar cross-section for the whole specimen (concrete and FRP); hence we named the corresponding model the LEFM–equivalent beam (LEFM–EB) model. Since $\beta \propto \sqrt{k}$ (Eq. (12)), the LEFM–EB model can be seen as a particular case of the softening models assuming both $\alpha \rightarrow \infty$ (brittle interfacial behaviour) and $\beta \rightarrow \infty$ (rigid interface). However, the analytical results provided by the LEFM–EB model can be obtained much more easily by directly applying Eq. (39). We simply need to evaluate the strain energy release rate. To this aim, note that Eq. (38) is useless in the present case, since both the maximum shear stress τ_{\max} and the shear stiffness k diverge and Eq. (38) becomes an undetermined expression. On the other hand, the strain energy release rate can be straightforwardly obtained by a simple energy balance, as reported in Appendix D.

According to the LEFM–EB model, the load vs. displacement plot is represented (see Fig. 8) by a triangle, made of: (i) a vertical (rigid) line up to the debonding onset, corresponding to the maximum transferable load; (ii) a flat line, i.e. at constant load, up to final debonding; (iii) a linear unloading back to the origin. With respect to the previous models, the LEFM–EB one is the simplest, being characterised only by the mode II fracture energy \mathcal{G}_{IIc} .

In Figs. 8–9, we plotted the load–displacement curves provided by the four bond–slip models according to different values of the parameters α and β . First of all, it is worth noting that the area beneath the different curves in each plot as well as the slope at the origin are the same, since all the models are characterised by the same fracture energy \mathcal{G}_{IIc} and elastic stiffness k (except the LEFM–EB model, for which $k \rightarrow \infty$). Then note that the exponential softening model is the one providing the lowest load predictions, at least in the first part of the plot. From the most to the least conservative, we can list the four models as follows: exponential softening, linear softening, LEFM, LEFM–EB. If the exponential softening is the one describing more realistically the behaviour of the interface, we can conclude that the linear softening model (and the LEFM models even more) tends to overestimate the maximum transferable force by the FRP.

From Fig. 8 it is also evident that softening interfaces generally predict the occurrence of snap-back instabilities, which disappear (see Fig. 8(a)) only for relatively low α and β values (i.e. relatively ductile interfaces and/or relatively short bond lengths). Note that, in the case of a linear softening interface, the threshold for the rising of snap-back instabilities can be set analytically: snap-back occurs whenever the product $\alpha \times \beta$ is larger than $\pi/2$ (see Appendix B for details).

Finally, for what concerns the differences between the softening models, it is seen that the exponential one differs from the linear one because of a stronger deviation from the initial slope of the ascending branch. Furthermore, a residual – although small – transferable force is present also for large displacements because of the exponentially decaying shear stress.

As expected, the strongest differences between softening models and LEFM models are achieved for small α and β values. From Fig. 9(a) it is clear that the softening models merge with the LEFM model for sufficiently large α values (for any β), whereas they all collapse onto the LEFM–EB model if β is sufficiently large as well.

6. Parametric analysis

In the present section we perform a parametric analysis of the pull–push shear test based on the interface cohesive law with an exponential softening presented in Section 3 and on the analytical solution obtained in Section 4.

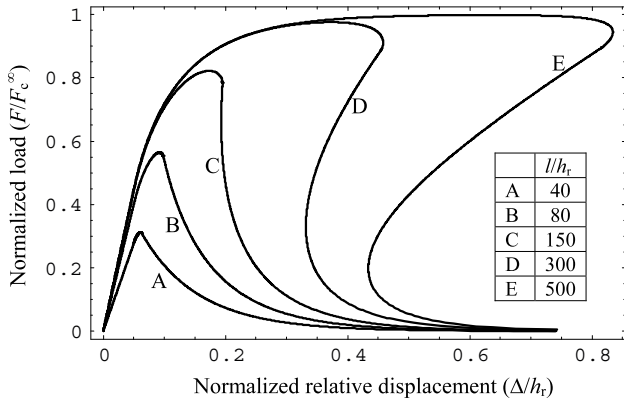


Fig. 10. Effect of the bond length on load vs. displacement curve. Dimensionless ratios equal to $h_b/h_r = 100$; $t_r/h_r = 25$; $t_b/h_r = 100$; $E_r/\tau_p = 62, 500$; $E_b/\tau_p = 7500$; $\alpha = 0.5$; $s_E = 0.125$.

Taking as fundamental quantities the peak stress τ_p and the thickness of the FRP plate h_r , dimensional analysis shows that, during the debonding process, the dimensionless load and edge displacement depend on the following dimensionless ratios:

$$\left. \begin{array}{l} \frac{F}{\tau_p h_r^2} \\ \frac{\Delta}{h_r} \end{array} \right\} = f \left(\frac{t_b}{h_r}; \frac{t_r}{h_r}; \frac{h_b}{h_r}; \frac{l}{h_r}; \frac{E_r}{\tau_p}; \frac{E_b}{\tau_p}; \alpha; \frac{\mathcal{G}_{IIc}}{\tau_p h_r} \right). \quad (40)$$

We define the last ratio, ruling the size effect, as the interface energetic brittleness number s_E :

$$s_E = \frac{\mathcal{G}_{IIc}}{\tau_p h_r}. \quad (41)$$

This represents the extension to mode II debonding failure of the energetic brittleness number $\mathcal{G}_F/(\sigma_u h)$ introduced by Carpinteri [15,22] for homogeneous quasi-brittle materials (\mathcal{G}_F being the mode I fracture energy and σ_u the tensile strength).

6.1. Effect of the bond length

In Fig. 10 we fixed all the parameters in Eq. (40) except the ratio of the bond length l to the thickness of the FRP plate h_r . For the sake of clarity, the load is normalised with respect to F_c^∞ instead of $\tau_p h_r^2$. It is evident that, increasing the bond length, the elastic stiffness as well as the maximum load tend to a constant value. More in detail, the maximum transmissible force is F_c^∞ , while the structural behaviour changes from quasi-brittle (curve A) to ductile–brittle (curve E). Note that, for relatively large bond lengths (curves C–D–E), a snap-back instability occurs. Finally, it is worth observing that, based on Fig. 10, it is possible to define an effective bond length, i.e. a threshold length, beyond which the maximum load is practically equal to F_c^∞ .

6.2. Effect of FRP stiffness

In Fig. 11 we fixed all the parameters in Eq. (40) except the ratio between the Young’s moduli of the FRP and of the concrete, i.e. E_r/E_b . Note that the same effect is obtained by varying h_r/h_b . It is seen that, increasing the reinforcement stiffness, the maximum load increases as well as the brittleness of the structural response. In more detail, the structural behaviour changes from quasi-brittle (curve A) to ductile–brittle (curve E). Note that, for relatively low FRP stiffnesses (curves C–D–E), the structural response is ductile up to a final snap-back instability. Eventually, it is worth observing that the area beneath each curve, which is proportional to the

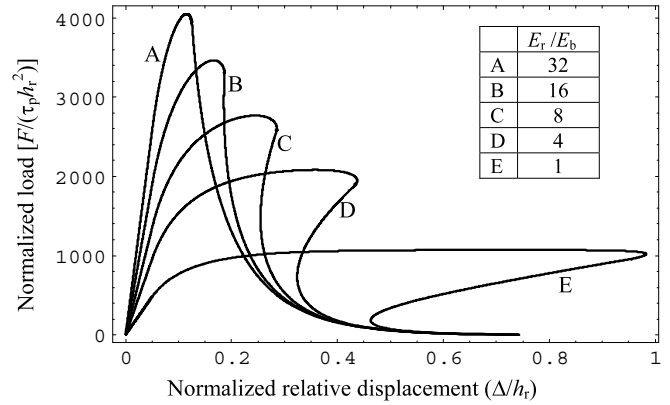


Fig. 11. Effect of the FRP stiffness on load vs. displacement curve. Dimensionless ratios equal to $h_b/h_r = 100$; $t_r/h_r = 25$; $t_b/h_r = 100$; $l/h_r = 200$; $E_b/\tau_p = 7500$; $\alpha = 0.5$; $s_E = 0.125$.

energy spent to have complete delamination, is constant and that, for high FRP stiffnesses, the effective bond length increases.

6.3. Effect of the interfacial cohesive law

We wish now to analyse the effect of the shape of the cohesive law, within the assumption of a linear ascending branch followed by an exponential tail (Eq. (8)). We consider two cases. In the former one, we keep τ_p and δ_p constant and let α vary (and s_E accordingly), see Fig. 12(a). All the other dimensionless ratios (Eq. (40)) are kept constant. Although τ_p is the same for all the curves, from Fig. 12(b) it is evident that the presence of a softening branch gives rise to a strength supply beyond the elastic regime. In fact, the load at which the stress reaches τ_p at the loaded end is also the maximum load only for an elastic–perfectly brittle interface (curve A). On the other hand, the softening of the interface cohesive law makes the maximum load higher (curves B–C–D) and a horizontal plateau is reached for an elastic–perfectly plastic interface (curve E). Eventually, observe that a snap-back instability occurs only for strongly decaying softening branches, i.e. for relatively high α values (curves A–B–C).

In the latter case, we keep \mathcal{G}_{IIc} and k constant and let α vary (and s_E accordingly), see Fig. 13(a). All the other dimensionless ratios (Eq. (40)) are kept constant. Since now τ_p is varying, it is more convenient to normalise the load with respect to F_c^∞ instead of $\tau_p h_r^2$. Fig. 13(b) shows that, for a given bond length, the maximum transmissible force F_c^∞ is attained only by the curves corresponding to rapidly decreasing softening branches. Note that, k being constant, the initial (elastic) slope of the F – Δ curves is the same for all the curves; analogously, the area beneath each curve is constant since the energy required to have complete delamination is the same ($\mathcal{G}_{IIc} \times t_r \times l$). The snap-back instability disappears for very slowly decreasing softening branches (curve E), when the F – Δ curve early departs from the initial (elastic) straight line.

6.4. Size-scale effect

In Fig. 14 we fixed all the parameters in Eq. (40) except the interface energetic brittleness number s_E . Varying s_E means, for instance, that the overall structural size changes while keeping constant all the geometrical ratios and material properties. Therefore, Fig. 14 describes the size-scale effect for the pull–push shear test. It shows that, increasing the interface energetic brittleness number, the structural behaviour changes from ductile–brittle to quasi-brittle and that the snap-back instability occurs for relatively low s_E values. It is important to highlight that brittleness is not a purely

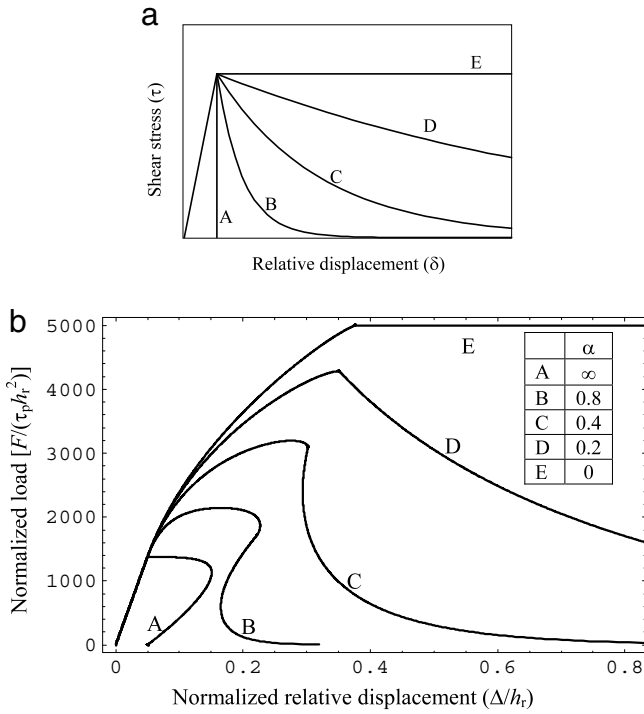


Fig. 12. Effect of the interface law (a) on the load vs. displacement curve (b) by varying α and keeping τ_p and δ_p constant. Dimensionless ratios equal to $h_b/h_r = 100$; $t_r/h_r = 25$; $t_b/h_r = 100$; $l/h_r = 200$; $E_r/\tau_p = 62, 500$; $E_b/\tau_p = 7500$; $s_E = (1 + \alpha^2)/(2\alpha^2) \times 5 \times 10^{-2}$, i.e. $\delta_p/h_r = 0.05$.

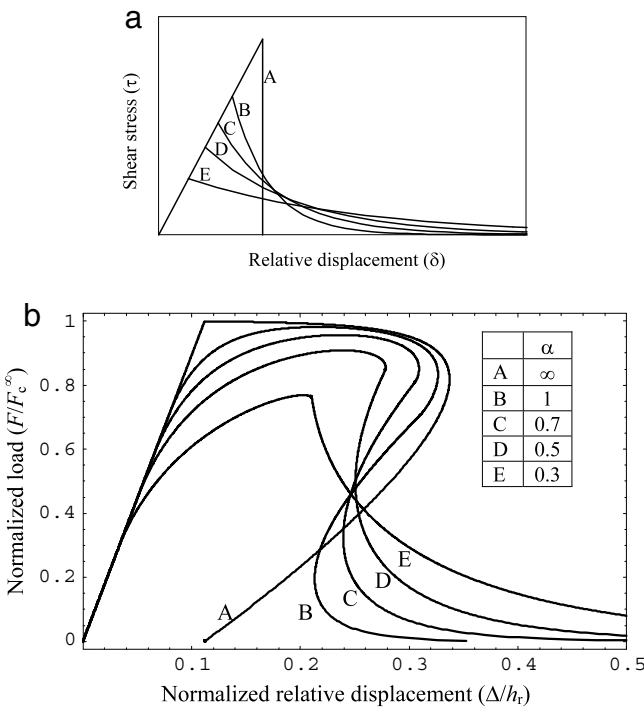


Fig. 13. Effect of the interface law (a) on the load vs. displacement curve (b) by varying α and keeping k and \mathcal{G}_{ilc} fixed. Dimensionless ratios equal to $h_b/h_r = 100$; $t_r/h_r = 25$; $t_b/h_r = 100$; $l/h_r = 200$; $E_r h_r/\mathcal{G}_{ilc} = 5 \times 10^5$; $E_b h_r/\mathcal{G}_{ilc} = 6 \times 10^4$; $s_E = [5(1 + \alpha^2)]^{1/2}/(40\alpha)$, i.e. $kh_r^2/\mathcal{G}_{ilc} = 160$.

material property, but a structural one: in fact, low interface energetic brittleness numbers correspond to brittle interfaces and/or

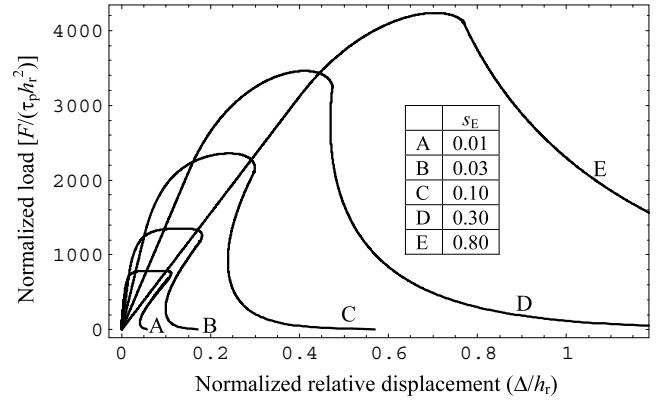


Fig. 14. Size effect on load vs. displacement curve. Dimensionless ratios equal to $h_b/h_r = 100$; $t_r/h_r = 25$; $t_b/h_r = 100$; $l/h_r = 200$; $E_r/\tau_p = 62, 500$; $E_b/\tau_p = 7500$; $\alpha = 0.5$.

large sizes, while high s_E values correspond to ductile interfaces and/or relatively small sizes.

7. Comparison with experimental results

In the experimental tests, usually the load is not applied at the beginning of the bonded region of the FRP plate, but at a certain distance from the concrete block (see Fig. 15), hereafter denoted by l_0 . In such a case, the recorded displacement Δ is given by the increment of the distance between the contrast point (i.e. the edge of the concrete block) and the loaded point of the FRP plate. Hence the formulae for the construction of the load–displacement curve provided in Section 4 have to be updated by adding the elastic elongation of the free portion of FRP plate:

$$\Delta_0 = \frac{Fl_0}{E_r h_r t_r} \quad (42)$$

which, in dimensionless form, reads:

$$\frac{\Delta_0}{\delta_p} = \frac{F}{F_c^\infty} \frac{\beta \lambda_0 \sqrt{1 + \alpha^2}}{\alpha (1 + \rho)} \quad (43)$$

where the dimensionless quantity $\lambda_0 = l_0/l$ has been introduced. The contribution (43) has to be added in the first equations of the systems (20), (28) and (33), the ratio F/F_c^∞ in Eq. (43) being provided by the second equations of the same systems. Since the additive term is proportional to the load F and to the free length l_0 , it is evident that the application of the load at a distance l_0 increases the possibility to have a snap-back instability under displacement control and that the occurrence of the snap-back is higher for larger free lengths l_0 .

In order to prove the soundness of the present model, we provide a comparison with some experimental data obtained by Yao et al. [23]. They performed an extensive experimental program, regarding carbon FRP strips bonded to concrete blocks. In total, they prepared 72 specimens to perform single pull–push shear tests. Herein we consider the results obtained from the specimens of the Series VII, for which the failure mode is homogeneous, being represented by cracking of concrete few millimetres from the adhesive–concrete separation surface. In more detail we considered the tests on specimens 2, 3, 6, 7 of the Series VII, corresponding to bond lengths l equal to 95, 145, 190 and 240 mm respectively; l_0 is equal to 50 mm.

The concrete block has cross section of dimensions $h_b = 150$ mm and $t_b = 150$ mm. The Young’s modulus of concrete, slightly affecting the results, is supposed to be equal to 30 GPa. The geometrical and elastic properties of the carbon FRP plates are the following: $h_r = 0.165$ mm, $t_r = 25$ mm, $E_r = 256$ GPa.

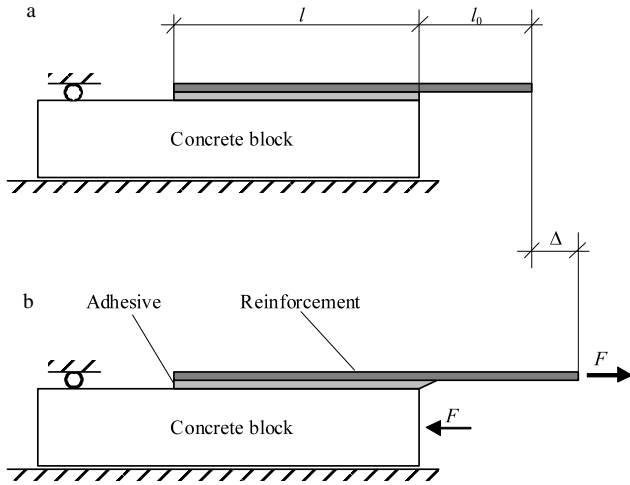


Fig. 15. Experimental setup for the single pull–push shear test geometry: unloaded (a) and loaded (b) schemes. The load is applied to the FRP plate at a distance l_0 from the concrete block.

Cottone and Giambanco [17] fitted the same tests by the linear softening model. By means of an original identification procedure, they obtained the following values for the interface parameters: peak stress τ_p equal to 4.20 MPa; slope of the softening branch ($k\alpha^2$) equal to 9.50 N/mm³; slope of the elastic branch (k) equal to 48, 36, 160, 40 N/mm³ for specimen 2, 3, 6, 7 of the Series VII, respectively. The high k value for the specimen VII-6 is probably related to a different procedure adopted for the hand lay-up.

In Fig. 16 the load–displacement curves for the different values of the bond length, obtained by the exponential and the linear softening models as well as by the LEFM model, are illustrated and compared with the experimental data. A satisfactory agreement between the experimental response and exponential softening model predictions can be noticed in terms of elastic behaviour, departure from linearity and maximum transferable force. As expected, LEFM provides quite rough predictions. For what concerns softening models, it is seen that, despite the identification procedure being based on the linear softening model, in three cases out of four (Fig. 16(a), (b) and (d)) the exponential softening model is the one providing the best fit. Particularly, the exponential model proposed in the present paper seems to catch better the (stronger) deviation from linearity of the experimental data after the elastic stage.

8. Conclusions

In the present paper a closed-form solution describing the full-range behaviour of FRP-to-concrete bonded joints is presented. Restricting the analysis to the pull–push geometry, a dimensional and parametrical analysis of the problem has been performed, highlighting the effects on the solution of the bond length, the FRP stiffness, and the interface law. Moreover, the size effect for the problem under examination has been addressed. A comparison with some experimental data available in literature concludes the paper.

Concerning the comparison with different models available in the literature, it is worth observing that: (i) models neglecting the interface nonlinearity (i.e. models accounting for an elastic-perfectly brittle interface law) usually provide very rough predictions; (ii) with respect to the linear softening model, the present model is believed to be more realistic and, at the same time, easier to be implemented (only 3 stages out of 4); (iii) since the exponential softening model provides the most conservative failure load predictions, application of linear softening or LEFM models

is potentially dangerous; (iv) with respect to more sophisticated local bond–slip models (such as the one proposed by Ferracuti et al. [24]), the present approach provides similar results without needing a proper numerical analysis. Of course, the present analysis is restricted to a specific geometry (i.e. the pull–push shear test), but the approach is general: the solution procedure outlined can be easily extended to deal with similar test setups, such as the pull–pull shear test. These extensions, as well as the comparison with other analytical models for FRP debonding such as the three-parameter model by Leung and Tung [7], will be the matter of future developments.

Acknowledgements

The financial support of the Italian Ministry of Education, University and Research (MIUR) to the Project “Advanced applications of fracture mechanics for the study of integrity and durability of materials and structures” within the “Programmi di ricerca scientifica di rilevante interesse nazionale (PRIN)” program for the year 2008 is gratefully acknowledged.

Appendix A

In this appendix we provide the analytical details leading to the solutions represented by Eqs. (25) and (30).

The differential problems set in Eqs. (24) and (29) are particular cases of the following initial value problem:

$$\begin{cases} \frac{d^2y}{dx^2} = f(y) \\ y(x_0) = y_0 \\ y'(x_0) = y_1 \end{cases} \quad (\text{A.1})$$

where $y(x)$ is the unknown function. By multiplying both sides of the differential equation in (A.1) times the first derivative dy/dx and by introducing the primitive $F(y)$ of $f(y)$ (i.e. $dF/dy = f(y)$), we get:

$$\frac{d}{dx} \left[\frac{1}{2} \left(\frac{dy}{dx} \right)^2 \right] = \frac{dF}{dx} \quad (\text{A.2})$$

yielding:

$$\frac{dy}{dx} = \pm \sqrt{2F(y) + \text{const.}} \quad (\text{A.3})$$

Assuming the positivity of the first derivative and exploiting the initial conditions in (A.1), we can determine the constant so that Eq. (A.3) becomes:

$$\frac{dy}{dx} = \sqrt{y_1^2 + 2[F(y) - F(y_0)]}. \quad (\text{A.4})$$

Separating the variables and integrating yields:

$$x - x_0 = \int_{y_0}^y \frac{dy}{\sqrt{y_1^2 + 2[F(y) - F(y_0)]}} \quad (\text{A.5})$$

which provides in implicit form the desired function $y(x)$.

In the considered cases (Eqs. (24) and (29)), the function $f(y)$ is given by the second function in Eq. (10). Its primitive reads:

$$F(y) = -\frac{\beta^2}{2\alpha^2} e^{-2\alpha^2(y-1)}. \quad (\text{A.6})$$

Firstly, let us consider the initial value problem set in Eq. (24), that is, in the elastic-softening stage. In such a case Eq. (A.5) becomes:

$$\xi - \bar{\xi} = \int_1^y \frac{\alpha}{\beta \sqrt{\gamma^2 - e^{-2\alpha^2(y-1)}}} dy \quad (\text{A.7})$$

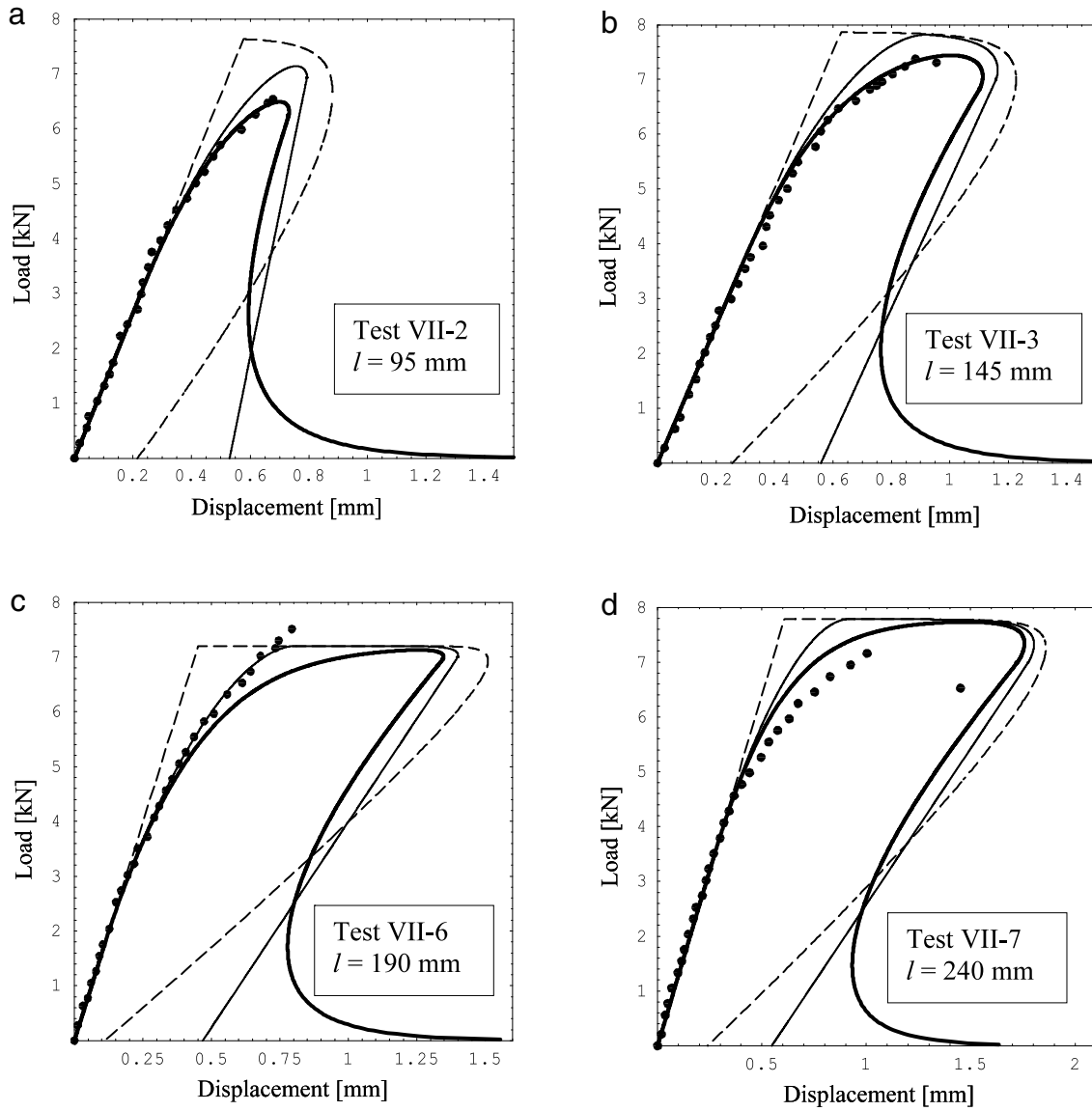


Fig. 16. Comparison between experimental data (black dots) and theoretical predictions: exponential softening (thick line), linear softening (thin line), LEFM (dashed line). Plots from (a) to (d) refer to specimens with different bond lengths (see legend).

where $\gamma = [\alpha^2 \tanh^2(\beta\bar{\xi}) + 1]^{1/2}$. The integral in Eq. (A.7) can be achieved in closed form. Thus:

$$\xi - \bar{\xi} = \frac{1}{\alpha\beta\gamma} \ln \frac{\gamma e^{\alpha^2(y-1)} + \sqrt{\gamma^2 e^{2\alpha^2(y-1)} - 1}}{\gamma + \alpha \tanh(\beta\bar{\xi})}. \quad (A.8)$$

By some analytical manipulations it is then possible to explicitly define y as a function of ξ :

$$y(\xi) = 1 + \frac{1}{\alpha^2} \ln \frac{\alpha^2 \tanh^2(\beta\bar{\xi}) e^{\alpha\beta\gamma(\xi-\bar{\xi})} + e^{-\alpha\beta\gamma(\xi-\bar{\xi})}}{2\gamma\alpha \tanh(\beta\bar{\xi})}. \quad (A.9)$$

By exploiting the properties of the hyperbolic cosine, Eq. (25) is finally recovered from Eq. (A.9). Then Eq. (26) follows by derivation.

We can proceed analogously to solve the differential problem in the fully softening stage represented by Eq. (29). In such a case Eq. (A.5) becomes:

$$\bar{\xi} = \int_{1-\frac{\ln v}{2\alpha^2}}^y \frac{\alpha}{\beta\sqrt{v} - e^{-2\alpha^2(y-1)}} dy. \quad (A.10)$$

Integrating:

$$\alpha\beta\bar{\xi}\sqrt{v} = \ln \left[\sqrt{v} e^{\alpha^2(y-1)} + \sqrt{v e^{2\alpha^2(y-1)} - 1} \right]. \quad (A.11)$$

By making explicit the dependence of y on ξ :

$$y(\xi) = 1 + \frac{1}{\alpha^2} \ln \frac{e^{\alpha\beta\bar{\xi}\sqrt{v}} + e^{-\alpha\beta\bar{\xi}\sqrt{v}}}{2\sqrt{v}}. \quad (A.12)$$

Eventually, Eq. (30) is recovered by properly introducing the hyperbolic cosine into Eq. (A.12).

Appendix B

In this appendix the formulae providing the load vs. displacement curve for a pull–push shear test assuming a linear softening interface law are given according to the symbols used in the present paper. They are introduced for the sake of completeness and to highlight the differences with the exponential softening model dealt in the present paper. Formulae within this appendix have been exploited to plot the corresponding curves in Figs. 8–9 and 16.

According to the linear softening law, two different solutions may take place depending whether the dimensionless parameter ψ is larger or lower than unity, ψ being equal to:

$$\psi = \frac{\pi}{2\alpha\beta}. \tag{B.1}$$

Let us consider firstly the (more usual) case $\psi < 1$ (Fig. 8(b), (c) and (d)), occurring for relatively large bond lengths (high β) and/or brittle interface (high α). Of course the elastic stage (first stage) coincides with the one considered in the present paper (Eq. (20)). For what concerns the elastic-softening (second) stage, we have:

$$\begin{cases} \frac{\Delta}{\delta_p} = 1 + \frac{1}{\alpha^2} \\ \quad \times \{1 - \cos[\alpha\beta(1 - \bar{\xi})] + \alpha \tanh(\beta\bar{\xi}) \sin[\alpha\beta(1 - \bar{\xi})]\} \\ \frac{F}{F_c^\infty} = \frac{1}{\sqrt{1 + \alpha^2}} \\ \quad \times \{ \sin[\alpha\beta(1 - \bar{\xi})] + \alpha \tanh(\beta\bar{\xi}) \cos[\alpha\beta(1 - \bar{\xi})] \}. \end{cases} \tag{B.2}$$

In Eq. (B.2) the parameter $\bar{\xi}$ defines, as in Eq. (28), the relative position of the peak stress. It ranges from 1 to ξ_{23} , i.e. $\xi_{23} < \bar{\xi} < 1$. ξ_{23} is the position of the peak stress at the debonding onset, i.e. when the second stage ends and the third one begins. ξ_{23} must be achieved by numerically solving the following transcendental equation:

$$\alpha \tanh(\beta\xi_{23}) \tan[\alpha\beta(1 - \xi_{23})] = 1 \tag{B.3}$$

where the root closer to unity must be chosen if multiple solutions are available. When $\bar{\xi}$ reaches ξ_{23} , the interface enters the elastic-softening-debonding (third) stage, when all the phases coexist along the joint length. In this case the load–displacement curve is provided by:

$$\begin{cases} \frac{\Delta}{\delta_p} = \left(1 + \frac{1}{\alpha^2}\right) + \frac{\beta}{\alpha} \frac{1 - \xi_d}{\sin[\alpha\beta(\xi_d - \bar{\xi})]} \\ \frac{F}{F_c^\infty} = \frac{1}{\sqrt{1 + \alpha^2} \sin[\alpha\beta(\xi_d - \bar{\xi})]} \end{cases} \tag{B.4}$$

where the relative position $\bar{\xi}$ of the peak stress travels from ξ_{23} to 0: $0 < \bar{\xi} < \xi_{23}$. ξ_d is the active fraction of the bond length, i.e. the relative distance between the debonded zone and the unloaded end. Its value is:

$$\xi_d = \bar{\xi} + \frac{1}{\alpha\beta} \arctan \frac{1}{\alpha \tanh(\beta\bar{\xi})}. \tag{B.5}$$

When the peak stress reaches the unloaded extreme ($\bar{\xi} = 0$), the interface enters the softening–debonding (fourth) stage. During this stage the relative active length ξ_d remains constant and equal to ψ up to complete debonding; the load–displacement curve is provided by:

$$\begin{cases} \frac{\Delta}{\delta_p} = \left(1 + \frac{1}{\alpha^2}\right) + \frac{\beta}{\alpha} \left(1 - \frac{\pi}{2\alpha\beta}\right) v \\ \frac{F}{F_c^\infty} = \frac{v}{\sqrt{1 + \alpha^2}} \end{cases} \tag{B.6}$$

where, as in Eq. (33), v is the ratio of the shearing stress to the peak stress at the unloaded end. When $v = 0$, the FRP plate is completely detached from the concrete substrate.

Now, let us consider the latter case, i.e. $\psi > 1$ (Fig. 8(a)), corresponding to very short bond lengths (low β) and/or relatively ductile interfaces (low α). In such a case the coexistence of the three phases (elastic, softening and debonded) never occurs, i.e. the third stage is skipped. In other words, the elastic-softening (second) stage described by Eq. (B.2) holds for the entire interval

$0 < \bar{\xi} < 1$. When the peak stress reaches the unloaded extreme ($\bar{\xi} = 0$), the interface enters directly the softening stage, described now by the following relationships:

$$\begin{cases} \frac{\Delta}{\delta_p} = \left(1 + \frac{1}{\alpha^2}\right) - v \frac{\cos(\alpha\beta)}{\alpha^2} \\ \frac{F}{F_c^\infty} = v \frac{\sin(\alpha\beta)}{\sqrt{1 + \alpha^2}} \end{cases} \tag{B.7}$$

replacing the previous (B.6). As above, v ranges from 1 to 0. Note that in this case debonding is achieved simultaneously upon the whole bond length when $v \rightarrow 0$.

It is worth observing that, whatever is the ψ -value, the load–displacement plot during the softening stage (described either by Eq. (B.6) or by Eq. (B.7)) corresponds to a straight line, i.e. a linear unloading is always predicted by the model. However, its slope is positive if $\psi < 1$ (as in Fig. 8(b), (c) and (d)) and negative if $\psi > 1$ (as in Fig. 8(a)). It means that a snap-back instability occurs only for $\psi < 1$. In the limit case $\psi = 1$, a vertical drop of the load at constant displacement is predicted by the linear softening interface model.

In case the load is applied at a distance l_0 from the concrete block (Fig. 15), analogously to that done for the exponential softening model, the quantity (43) has to be added to the first equations in the systems (B.2), (B.4), (B.6) and (B.7). In such a case, snap-back instability is more likely to occur and the condition for the presence of the snap-back reads now $\psi < \bar{\psi}$, where $\bar{\psi} > 1$ is the solution of the transcendental equation:

$$\frac{\pi}{2\bar{\psi}} \tan\left(\frac{\pi}{2\bar{\psi}}\right) = \frac{1 + \rho}{\lambda_0}. \tag{B.8}$$

For what concerns the comparison with the experimental data performed in the paper, it is worth observing that only the test with the shortest bond length (i.e. specimen VII-2) was characterised by a ψ -value larger than unity and Eqs. (B.2) and (B.7) have been used accordingly to plot the corresponding curve in Fig. 16(a). In all the other cases (Fig. 16(b), (c) and (d)), Eqs. (B.2), (B.4) and (B.6) has been used instead.

As a final comment, we wish to emphasise that, beyond being more realistic, the solution based on the exponential softening is achieved more easily with respect to the one based on a linear softening branch. In fact, in the linear softening case: (i) the solution is generally made of four stages instead of three (ii) the solution is not fully analytical since Eq. (B.3) has to be solved numerically (iii) a distinction has to be made between the case $\psi < 1$ and $\psi > 1$, whereas the exponential model is insensitive to the ψ value.

Appendix C

In this appendix we provide the formulae describing the load vs. displacement curve for a pull–push shear test assuming a linear elastic-perfectly brittle interface (LEFM model). Formulae within this appendix have been exploited to plot the corresponding curves in Figs. 8–9 and 16.

According to the LEFM model (i.e. Eqs. (38)–(39)), the failure load is achieved when the maximum shearing stress at the loaded end reaches its peak, which, as can be evinced from Fig. 7, is equal to $\sqrt{2g_{IIC}k}$. The failure load can hence be obtained from the linear elastic solution, namely from the second equation in the system (20), by setting $u = \sqrt{2g_{IIC}k}/\tau_p$ and replacing β with $\beta\bar{\xi}$ to take into account the decrease in the bonded length during delamination. Hence, by some analytical manipulation, we simply get:

$$\frac{F}{F_c^\infty} = \tanh(\beta\bar{\xi}). \tag{C.1}$$

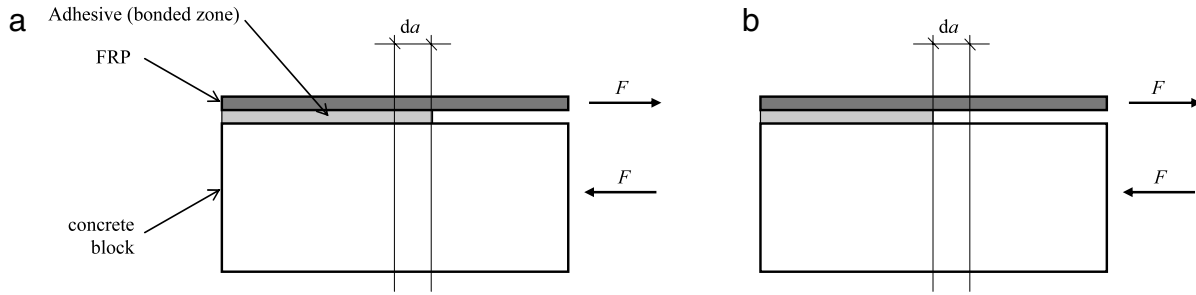


Fig. D.1. Equivalent beam (EB) model scheme for the evaluation of the strain energy release before (a) and after (b) an infinitesimal crack advancement (da).

Note that, in this case, the parameter $\bar{\xi}$, varying from 1 to 0, represents not only the position of the peak stress but also the fraction of the active portion of the interface (i.e. the ratio of the bond length during delamination to the initial bond length).

The corresponding displacement Δ is given by the sum of the relative displacement at the crack tip, always equal to $\sqrt{2g_{llc}/k}$, plus the elastic deformation of the FRP and concrete block:

$$\begin{aligned} \Delta &= \sqrt{2g_{llc}/k} + \frac{Fl(1-\bar{\xi})}{E_r h_r t_r} + \frac{Fl(1-\bar{\xi})}{E_b h_b t_b} \\ &= \sqrt{2g_{llc}/k} + \frac{Fl(1-\bar{\xi})}{E_r h_r t_r} (1 + \rho). \end{aligned} \quad (C.2)$$

Substituting Eq. (C.1) into (C.2), in dimensionless form we get:

$$\frac{\Delta}{\sqrt{2g_{llc}/k}} = 1 + \beta(1-\bar{\xi}) \tanh(\beta\bar{\xi}) \quad (C.3)$$

where it is evident that Δ is equal to $\sqrt{2g_{llc}/k}$ at the beginning and at the end of the delamination process ($\bar{\xi} = 1$ and $\bar{\xi} = 0$, respectively). In order to compare the LEFM model with the softening models, it is necessary to normalise the displacement at the loaded end Δ with respect to δ_p . The load–displacement curve is therefore represented by a straight line from the origin up to the maximum load followed by a softening branch described parametrically as follows:

$$\begin{cases} \frac{\Delta}{\delta_p} = \frac{\sqrt{1+\alpha^2}}{\alpha} [1 + \beta(1-\bar{\xi}) \tanh(\beta\bar{\xi})] \\ \frac{F}{F^\infty} = \tanh(\beta\bar{\xi}). \end{cases} \quad (C.4)$$

As above, if the load is applied at a distance l_0 from the concrete block (Fig. 15), the quantity (43) has to be added to the first equations in the systems (C.4).

Appendix D

In this appendix we provide the formulae describing the load vs. displacement curve for a pull–push shear test assuming a perfectly brittle as well as infinitely rigid interface (LEFM–EB model). Formulae within this appendix have been exploited to plot the corresponding curves in Figs. 8–9.

It is worth noting that the solution for the rigid–perfectly brittle interface can be seen as a particular case of the compliant interface solution. It is sufficient to let δ_p vanish and, at the same time, to let the stiffness k tend to infinity according to the relationship $k = 2g_{llc}/\delta_p^2$ (so that the mode II fracture energy is kept constant and equal to g_{llc}). However, it is also possible to obtain the failure load for the LEFM–EB model directly. In fact, a simple energy balance as the delamination crack increases by an infinitesimal step da yields:

$$d\phi = g_{llc} t_r da \quad (D.1)$$

where $d\phi$ is the difference in the elastic energy (at fixed load) after and before crack propagation in the da -wide strip (see Fig. D.1), since, outside the strip, the stress–strain state remains unchanged. In fact, because of the assumption of infinitely rigid interface, just beyond the delamination crack tip the specimen behaves as an equivalent beam. It means that, since the resultant axial force acting on the overall cross section is zero, beyond the tip also the stress and strain fields are zero. It follows that the strain energy in the strip before crack propagation is null and, therefore, the energy balance Eq. (D.1) yields:

$$\frac{F_c^2}{2E_r h_r t_r} da + \frac{F_c^2}{2E_b h_b t_b} da = g_{llc} t_r da. \quad (D.2)$$

From Eq. (D.2) the critical load can be obtained as:

$$F_c = t_r \sqrt{\frac{2g_{llc} E_r h_r}{1 + \rho}} \quad (D.3)$$

which coincides with the value reported in Eq. (13). Note that, while for highly compliant and/or ductile interfaces, this load may be reached only for sufficiently long bond lengths, for rigid interfaces the load (D.3) does not depend on the bond length. Therefore, according to the LEFM–EB model, the load–displacement is made of a vertical (rigid) branch up to delamination onset, followed by a horizontal line up to complete debonding when the displacement at the loaded end is:

$$\Delta = \frac{F_c l}{E_r h_r t_r} (1 + \rho). \quad (D.4)$$

Finally a linear unloading up to the origin concludes the diagram.

In order to compare the LEFM–EB predictions with the ones provided by the previous models, we have to normalise Eq. (D.4) with respect to δ_p . Hence, by means of Eq. (D.3), we get:

$$\frac{\Delta}{\delta_p} = \frac{\beta}{\alpha} \sqrt{1 + \alpha^2}. \quad (D.5)$$

In other words, the dimensionless load vs. displacement curve according to the LEFM–EB model is represented by a triangle whose vertices are (0, 0), (0, 1) and $(\beta\sqrt{1 + \alpha^2}/\alpha, 1)$ and that was plotted in Figs. 8–9.

References

- [1] Carpinteri A, Cornetti P, Lacidogna G, Paggi M. Towards a unified approach for the analysis of failure modes in FRP-retrofitted concrete beams. *Adv Struct Eng* 2009;12:715–29.
- [2] Teng JG, Smith ST, Yao J, Chen JF. Intermediate crack-induced debonding in RC beams and slabs. *Constr Build Mater* 2003;17:447–62.
- [3] Chen JF, Teng JG. Anchorage strength models for FRP and steel plates bonded to concrete. *J Eng Mech, ASCE* 2001;127:784–91.
- [4] Wu Z, Yuan H, Niu H. Stress transfer and fracture propagation in different kinds of adhesive joints. *J Eng Mech, ASCE* 2002;128:562–73.
- [5] Yuan H, Teng JG, Seracino R, Wu ZS, Yao J. Full-range behaviour of FRP-to-concrete bonded joints. *Eng Struct* 2004;26:553–65.

- [6] Leung CKY, Yang Y. Energy-based modelling approach for debonding of FRP plate from concrete substrate. *J Eng Mech, ASCE* 2006;132:583–93.
- [7] Leung CKY, Tung WK. Three-parameter model for debonding of FRP plate from concrete substrate. *J Eng Mech, ASCE* 2006;132:509–18.
- [8] Ferracuti B, Savoia M, Mazzotti C. A numerical model for FRP-concrete delamination. *Compos Part B Eng* 2006;37:356–64.
- [9] Suo Z, Hutchinson JW. Interface crack between two elastic layers. *Int J Fract* 1990;43:1–18.
- [10] Hart-Smith LJ. Adhesive-bonded double-lap joints. NASA contract report 112235; 1973.
- [11] Da Silva LFM, das Neves PJC, Adams RD, Spelt JK. Analytical models of adhesively bonded joints—part I: literature survey. *Int J Adhes Adhes* 2009;29:319–30.
- [12] Volkersen O. Die nietkraftverteilung in zugbeanspruchten Nietverbindungen mit konstanten laschen-querschnitten. *Luftfahrtforschung* 1938;15:4–47.
- [13] Neale KW, Ebead UA, Abdel Baky HM, Elsayed WE, Godat A. Analysis of the load-deformation behaviour and debonding for FRP-strengthened concrete structures. *Adv Struct Eng* 2006;9:751–63.
- [14] Lu XZ, Teng JG, Ye LP, Jiang JJ. Bond-slip models for FRP sheets/plates bonded to concrete. *Eng Struct* 2005;27:920–37.
- [15] Carpinteri A. Interpretation of the Griffith instability as a bifurcation of the global equilibrium. In: Shah SP, editor. *Application of fracture mechanics to cementitious composites*. Dordrecht: Martinus Nijhoff Publishers; 1985. p. 287–316.
- [16] Carpinteri A. Cusp catastrophe interpretation of fracture instability. *J Mech Phys Solids* 1989;37:567–82.
- [17] Cottone A, Giambanco G. Minimum bond length and size effects in FRP–substrate bonded joints. *Eng Fract Mech* 2009;76:1957–76.
- [18] Lenci S. Analysis of a crack at a weak interface. *Int J Fract* 2001;108:275–90.
- [19] Carpinteri A, Cornetti P, Pugno N. Edge debonding in FRP strengthened beams: stress versus energy failure criteria. *Eng Struct* 2009;31:2436–47.
- [20] Bennati S, Colleluori M, Corigliano D, Valvo PS. An enhanced beam-theory model of the asymmetric double cantilever beam (ADCB) test for composite laminates. *Compos Sci Technol* 2009;69:1735–45.
- [21] Távora L, Mantič V, Graciani E, Cañas J, París F. Analysis of a crack in a thin adhesive layer between orthotropic materials: an application to composite interlaminar fracture toughness test. *CMES Comput Model Eng Sci* 2010;58:247–70.
- [22] Carpinteri A. Static and energetic fracture parameters for rocks and concrete. *Mater Struct* 1981;14:151–62.
- [23] Yao J, Teng JG, Chen JF. Experimental study on FRP-to-concrete bonded joints. *Compos Part B Eng* 2005;36:99–113.
- [24] Ferracuti B, Savoia M, Mazzotti C. Interface law for FRP-concrete delamination. *Compos Struct* 2007;80:523–31.